UC San Diego
UC San Diego Previously Published Works

Title

Modified Coprecipitation Synthesis of Mesostructure-Controlled Li-Rich Layered Oxides for Minimizing Voltage Degradation

Permalink

Journal

ISSN

Authors

Zhang, Minghao
Liu, Haodong
Liu, Zhao
et al.

Publication Date

DOI

Modified Coprecipitation Synthesis of Mesostructure-Controlled Li-Rich Layered Oxides for Minimizing Voltage Degradation

Minghao Zhang,[†] Haodong Liu,[†] Zhao Liu,[‡] Chengcheng Fang,[†] and Ying Shirley Meng*,[†]

[†]Department of NanoEngineering, University of California San Diego, La Jolla, California 92093, United States
[‡]Department of Materials Science and Engineering, Northwestern University, Evanston, Illinois 60208, United States

S *Supporting Information*

ABSTRACT: Modified carbonate coprecipitation synthesis without addition of chelating agent is introduced to obtain mesostructure-controlled Li-rich layered oxides. The designed mesostructure for target material $Li_{1.2}Ni_{0.2}Mn_{0.6}O_2$ has uniformly dispersed spherical secondary particles with size around 3 μm. These micrometer-sized particles consist of self-assembled crystallites with size of ~150 nm. This unique design not only decreases the surface area compared with the sample with dispersive particles, but also increases overall structural mechanical stability compared with the sample with larger dense secondary particles as observed by transmission X-ray microscope. As a result, the voltage decay and capacity loss during long-term cycling have been minimized to a large extent. Our findings clearly demonstrate that mesostructure design of Li-rich layered oxides play a key role in optimizing this class of cathode materials. Surprisingly, the voltage fading issue can be partially mitigated by such an approach.

KEYWORDS: *mesostructure design, modified coprecipitation, Li-rich layered cathode, voltage decay mitigation, mechanical stability, Li-ion battery*
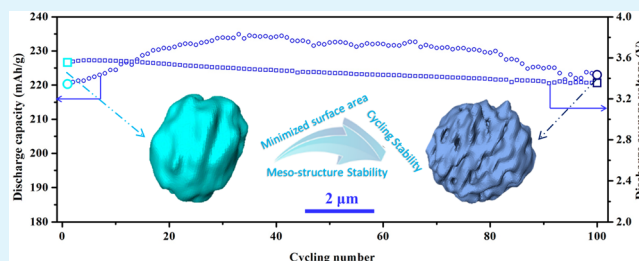
1. INTRODUCTION

With the expanding interest of variety of electric vehicles, lithium-ion battery with high energy density and long cycling life has to be accomplished, which drives the research and development of novel cathode materials. In this context, lithium-rich Mn-based layered oxides with composition $xLi_2MnO_3 \cdot (1-x)LiMO_2$ (M = Ni, Co, Mn, etc.) have been extensively investigated due to nearly doubled capacity compared with present cathode materials.[1−4] For example, $Li_{1.2}Ni_{0.2}Mn_{0.6}O_2$ and $Li_{1.2}Ni_{0.13}Co_{0.13}Mn_{0.54}O_2$ are able to deliver reversible capacities as high as 280 mAh g^{-1} in the voltage range between 2 and 4.8 V (vs Li$^+$/Li^0).[5,6] However, in order to achieve large-scale application of this material in commercial lithium-ion battery, several key problems and scientific challenges need to be solved and overcome. The first drawback is the irreversible voltage decay process during extended cycles. This voltage decay has been extensively investigated in the hope of identifying methods to mitigate the loss.[7−9]

As summarized in the previous review, synthesis methods have a distinct impact on the long-term cycling performances of this material because of differences in morphology and particle size.[10−13] Although various synthetic methods have been explored, the most commonly adopted method is liquid phase coprecipitation.[14,15] Coprecipitation synthesis for synthesis of Li-rich layered oxides, has many advantages: accurate precipitation of desired stoichiometric ratio; lower calcination temperature compared to solid-state method; and smaller primary particle size for better rate performance.[16−18] Depending on whether adding the chelating agent or not, two different types of samples can be obtained: (1) samples with dispersive particles (without mesostructure control) synthesized by the coprecipitation method without the chelating agent;[10] (2) large spherical morphology secondary particles comprised of nanosized primary particles when ammonium hydroxide is introduced in the coprecipitation method as a chelating agent.[19,20] With the ammonium hydroxide chelating agent, the average secondary particle size grows up to 20 μm which is composed of closely packed primary crystallites. The large size secondary particle, which is beneficial for tap density as well as energy density,[21] however, introduces kinetic limitations during first charging activation and high rate cycling.[22] And it was observed recently cracking of the large size secondary particles occurred during the initial charging process and could not fully recover after the discharging process, leading to capacity and voltage degradation over extended cycles.[23] Chen et al. also found internal cracks within these large size particles even before any electrochemical cycling, which causes cycling degradation.[24] Based on the above considerations, it would be meaningful to achieve homogeneous mesostructure-controlled precursors of Li-rich layered oxides, with smaller secondary particle size and improved mesostructure robustness.

In our present study, we introduce a modified coprecipitation (MCP) method to prepare mesostructure-controlled Li-rich layered oxide materials as high energy density cathodes for lithium ion batteries. This method is chelating agent free (without adding any ammonia), which is environmentally benign. More importantly, the obtained material $Li_{1.2}Ni_{0.2}Mn_{0.6}O_2$ has a unique mesostructure: (1) the secondary particles are spherical with uniform dispersion; (2) the secondary particles have a markedly reduced average diameter; (3) these ~3 μm secondary particles are composed of relatively loosely packed primary crystallites with size of ~150 nm. In this design, uniformly distributed small secondary particles not only have decreased the interface contact area with electrolyte, but also possess increased structure mechanical stability. Both features have positive effects on minimizing the voltage decay and capacity loss during long-term cycling of lithium-rich layered oxides.

2. EXPERIMENTAL SECTION

2.1. MCP Synthesis. As illustrated in Figure 1, a certain amount of Li_2CO_3 (carbonate ions: transitional metal ions = 1:1 in molar
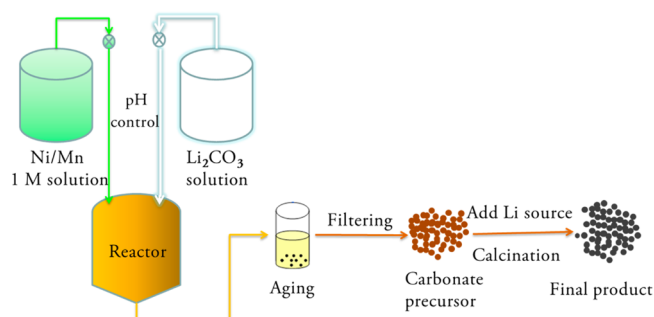

Figure 1. Schematic of the MCP synthesis process for mesostructure-controlled Li-rich layered oxides.

ratio) was dissolved in 60 mL deionized water. The Li_2CO_3 solution was then added into 10 mL solution of $Ni(NO_3)_2$ and $Mn(NO_3)_2$ with molar ratio 1:3 under stirring. To prevent hydroxide precursor from generating, pH value during coprecipitation process was carefully controlled. The obtained mixture was transferred to a 100 mL Teflon-lined stainless steel autoclave, and kept aging for 12 h at 80 °C. The resulting carbonate precursor was carefully washed with deionized water, and dried at 80 °C overnight. Thereafter, the dried powder was mixed with a certain amount of Li_2CO_3, and calcined at 500 °C for 5 h, and then sintered at 900 °C for 6 h followed by quenching in the air. Another sample with the same composition was also synthesized by a conventional coprecipitation (CCP) method without mesostructure control.[25] This CCP method without adding ammonia was adopted as a control experiment to exclude the influence of ammonium hydroxide on the electrochemical performance. The main difference between the two samples is mesostructure, which will be detailed in the Results and Discussion section.

2.2. Characterization of Materials. The crystal structure was characterized by X-ray diffraction (XRD) utilizing Bruker D8 advance diffractometer with copper Kα source. Rietveld refinement was applied to the obtained diffraction pattern using FullProf software. The morphology of the particle was identified by using FEI XL30 ultrahigh-resolution scanning electron microscope (UHR SEM) with an accelerating voltage of 10 kV. Surface area was determined using nitrogen physisorption by the Brunauer−Emmett−Teller (BET) method. ICP-OES was performed using a PerkinElmer 3700 optical emission plasma spectrometer. Tap densities were determined using a 10 mL graduated cylinder with 1000 taps.

Nanotomography measurement was operated at the beamline X8C, Brookhaven National Laboratory (BNL) through the transmission X-ray microscope (TXM).[26] 3D structure was reconstructed by a standard filtered back projection algorithm.[27] Tomography measurement with incident X-ray energy of 8400 eV was carried out in an absorption contrast mode to obtain the optimized image contrast for following imaging segmentation. Each tomographic data set was acquired over the angular range of 180° with a field of view of 40 × 40 μm^2 (the 2k × 2k CCD camera binned 2 × 2 pixels). Image processing includes reference correction, auto alignment, and magnification correction was carried out prior to tomographic reconstruction.[28]

2.3. Electrochemical Measurements. Electrochemical performances were measured on CR2016-type coin cells. The cathode electrodes were prepared by a mixture of the active materials, acetylene black, and polyvinylidene fluoride (PVDF) binder with a weight ratio of 80:10:10 on an aluminum foil. In order to remove the residue N-methyl-2-pyrrolidone (NMP) solvent, the electrode was dried in a vacuum oven at 80 °C for 12 h. Metallic lithium was used as the counter electrode, Celgard C480 membrane as the separator, and 1 M $LiPF_6$ dissolved in ethylene carbonate (EC)- dimethyl carbonate (DMC) with the volume ratio of 3:7 as electrolyte. The initial galvanstatic charge/discharge test was carried out at 0.05 C (1 C = 250 mAh g^{-1}) in the voltage range of 2.0−4.8 V. In the cyclic performance test, the cell was charged and discharged at 0.1 or 1.0 C, respectively. Electrochemical impedance measurement was performed on the Solartron 1287 electrochemical interface. The measurement was carried out in the frequency range of 0.01−100 000 Hz using a signal with an amplitude of 5 mV.

3. RESULTS AND DISCUSSION

3.1. Crystal Structure and Morphology Characterization. The XRD pattern of the precursor powder synthesized by our MCP method is shown in Figure S1. All the diffraction lines of the precursor can be indexed to a hexagonal $MnCO_3$ or $NiCO_3$ structure with space group $R\bar{3}c$, which indicates that a pure phase is acquired. The diffraction peaks are quite broad owing to the homogeneous nanosize particles as illustrated in Figure S2. On the basis of the ICP result, the formula of the carbonate precursor is determined as $(Ni_{0.25}Mn_{0.75})CO_3$.

Despite undergoing different synthesis routes, the final bulk crystal structure of products synthesized by the MCP and CCP method is quite similar to one another. Figure 2 shows the XRD pattern of $Li_{1.2}Ni_{0.2}Mn_{0.6}O_2$ sample synthesized by both methods. Except for peaks in 2θ range between 20° and 25°, all the other XRD peaks in both patterns can be corresponding to a rock salt structure with space group $R\bar{3}m$. The diffraction peaks between 20 and 25° are resulting from Li and Mn ordering in the transition metal layer, indicating the existence of Li_2MnO_3 component.[10] The peak separation of 006/012 and 018/110 reflections, as shown in Figure 2, suggests well-ordered layered structure is obtained from both methods.[29] And the value of intensity ratio $I(003)/I(104)$ are 1.52 and 1.51 for the sample synthesized by MCP and CCP method, respectively. This indicates a similar degree of Li/Ni cation mixing in the hexagonal layered structure.[30]

Rietveld refinement was performed on both samples using structural model $R\bar{3}m$. Note that the 2θ region between 20 and 25° was excluded in the reported Rietveld R-factor. The results of the refinement are listed in Table 1. The lattice parameters for both samples are almost identical to each other (within 0.1% differences). And furthermore, the refined Li/Ni mixing (number of Ni^{2+} on the Li$^+$ site) are exactly the same, 3.4% for both products. It confirms the qualitative interpretation of the
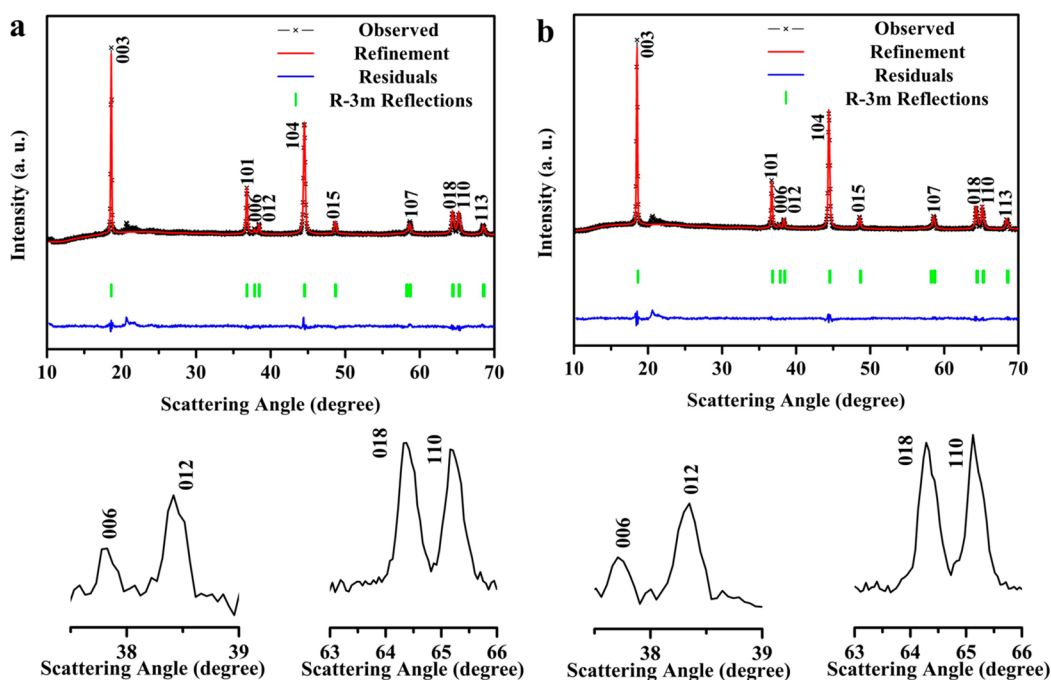
Figure 2. XRD spectra and Rietveld refinement of Li-rich layered oxide $Li_{1.2}Ni_{0.2}Mn_{0.6}O_2$ (a) synthesized by the MCP method with mesostructure control and (b) synthesized by the CCP method without mesostructure control. Enhanced view in the lower panel shows separation of each material's 006/012 and 018/110 peaks.

Table 1. Rietveld Fit Parameters of Li-Rich Layered Oxide $Li_{1.2}Ni_{0.2}Mn_{0.6}O_2$ Synthesized by the MCP and CCP Method

material	$a = b$ (Å)	c (Å)	z (O)	n Ni in Li layer	R_{wp} (%)	R_B (%)
MCP method	2.856(3)	14.241(8)	0.258(6)	0.034(3)	2.65	5.15
CCP method	2.854(7)	14.234(6)	0.257(6)	0.034(3)	2.39	4.20

similarity in crystallinity and bulk structure of the samples synthesized by the MCP and CCP method.

Despite their similar crystal structures, the samples prepared by different methods adopt significantly different morphologies. Figure 3a, b show SEM images for the $Li_{1.2}Ni_{0.2}Mn_{0.6}O_2$ powder synthesized by the MCP method. The obtained product has the spherical mesostructure with particle sizes ~2−3 μm. These microspherical particles consist of primary particles with size ~150 nm on average. This nanoparticles self-assembling process is well acknowledged under hydro-

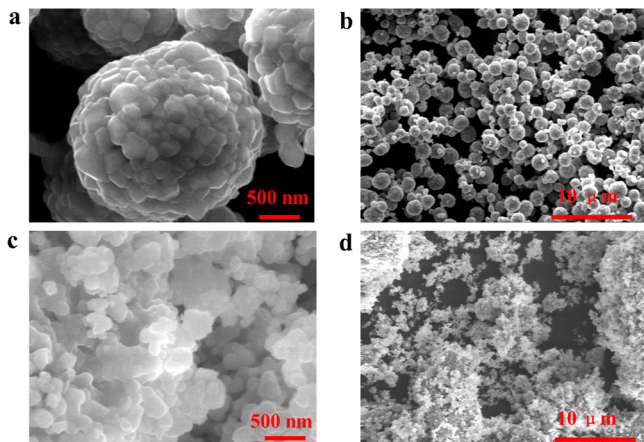thermal conditions.[31,32] The driving force for assembling nanoparticles into mesoscopic structures is the interface energy between nanoparticles. Under hydrothermal conditions, nano-crystallites (nucleation) agglomerate and form mesoporous spheres to minimize the system energy by decreasing the interfacial energy. At hydrothermal temperatures the nucleation process becomes faster than grain growth.[33] If there is no hydrothermal aging process, the grain growth rate will dominate the precipitation process, which creates less uniform secondary particles (see Figure S3). Note that the relatively lower hydrothermal temperature (80 °C) applied in the MCP method makes this synthesis is well-suited to potential large scale production. The tap density of the $Li_{1.2}Ni_{0.2}Mn_{0.6}O_2$ powder synthesized by the MCP method is ~1.95 g cm^{-3}, which is slightly lower than the commercial sample (~2.1 g cm^{-3}) with larger size secondary particles.[10] While, the sample synthesized by the CCP method consists of dispersive primary particles without well formed secondary particles, which brings about the increase of the specific surface area of the material. Table 2 shows that mesostructure-controlled material has the surface area, which is a half size (2.00 m^2 g^{-1}) of the material produced from the CCP method without mesostructure control (3.79 m^2 g^{-1}). Table 2 also experimentally confirms desired stoichiometric ratio between each element in targeting material is obtained from both methods. All the above characterization results demonstrate the crystallinity and chemical composition of the materials synthesized by different methods are quite similar, wheras the sample synthesized by the MCP method has a uniform spherical mesostructure and 2-

Figure 3. SEM images of Li-rich layered oxide $Li_{1.2}Ni_{0.2}Mn_{0.6}O_2$ synthesized by the (a, b) MCP and (c, d) CCP method.

Table 2. Surface area and Stoichiometry of Li-Rich Layered Oxide $Li_{1.2}Ni_{0.2}Mn_{0.6}O_2$ Synthesized by the MCP and CCP Method

material	surface area ($m^2 \ g^{-1}$)	stoichiometry	
		Mn:Ni	Li:(Mn+Ni)
theoretical		3:1	1.20:0.8
MCP method	2.00	2.98:1	1.21:0.8
CCP method	3.79	3.02:1	1.20:0.8

fold smaller surface area compared with the sample without mesostructure control synthesized by the CCP method.

3.2. Electrochemical Performance. Figure S4 shows the first-cycle voltage profile of $Li_{1.2}Ni_{0.2}Mn_{0.6}O_2$ cathode synthesized by the MCP method in the voltage between 2 and 4.8 V (vs Li^+/Li^0) at a current density of 12.5 mA g^{-1}. The charge curve consists of a slope region and a long plateau. The slope region is ascribed to the transition metal oxidation, Ni^{2+} oxidized to Ni^{4+} in this case.[34] And the plateau region is attributed to the oxygen oxidation and evolution from crystal lattice.[35] The mesostructure-controlled sample shows a high
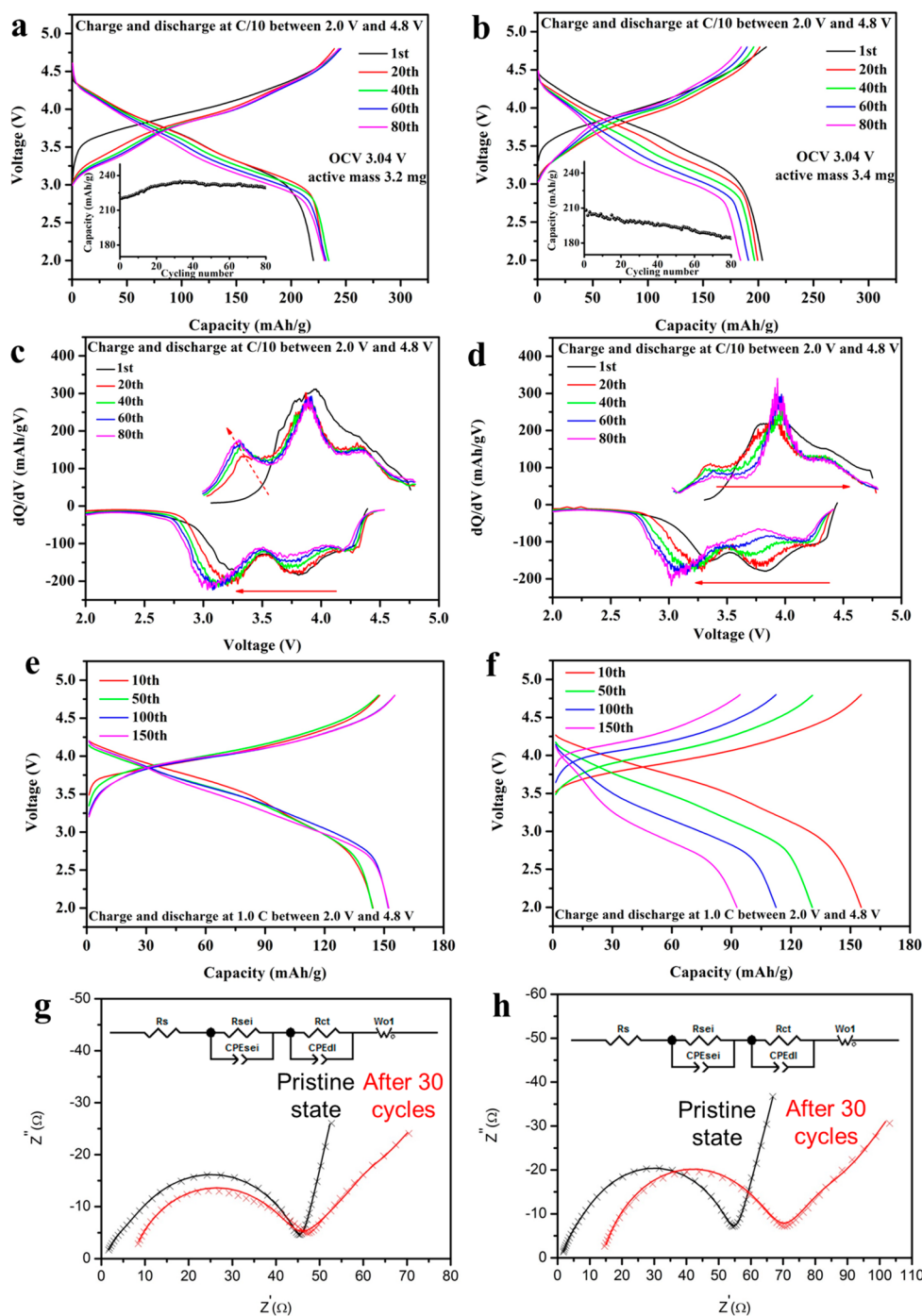

Figure 4. (a, b) First 80 electrochemical profiles, (c, d) corresponding dQ/dV plots, (e, f) cycling performance at higher rate, and (g, h) Nyquist fitting plots of Li-rich layered oxide $Li_{1.2}Ni_{0.2}Mn_{0.6}O_2$ synthesized by the (a, c, e, g) MCP and (b, d, f, h) CCP method.
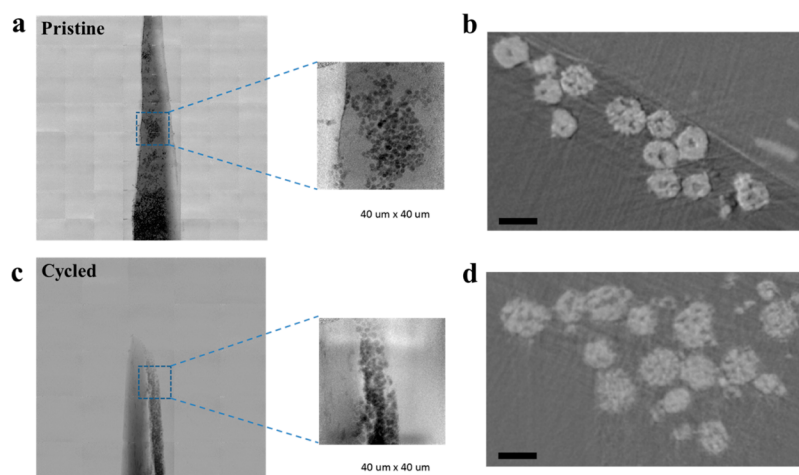
Figure 5. (a, c) TXM mosaic image projection and (b, d) 2D representative reconstructed slice of Li-rich layered oxide $Li_{1.2}Ni_{0.2}Mn_{0.6}O_2$ synthesized by the MCP method for (a, b) the pristine electrode and (c, d) cycled electrode. The scale bar is 2 μm.

discharge capacity of ~250 mAh g^{-1} at 0.05 C rate for the first cycle. And no obvious difference is found from the first cycle between the Li-rich layered oxide synthesized by the MCP and CCP method (see Figure S4b).

Figure 4a, b demonstrate changes in capacity and voltage during 80 cycles under the current density of 25 mA g^{-1} of both samples. To highlight the capacity loss and voltage degradation in different voltage regime, Figure 4c and d also show differential capacity, dQ/dV, for both samples. Clearly, all the capacity fade during discharge occurs beyond 3.6 V. Voltage degradation is present mainly in the low voltage regime, where dQ/dV peaks, near 3.8 and 4.3 V, do not shift obviously. Compared with the sample without mesostructure control, the mesostructure-controlled sample not only shows a large discharge capacity (220 mAh g^{-1}) at the first cycle, but also it exhibits almost the same capacity and voltage curve after 80 cycles. At higher rate such as 1.0 C, the mesostructure-controlled material still exhibits better cycling performance as shown in Figure 4e, f. The increasing capacity over cycles (initial activation process) is due to the low lithium diffusivity in bulk structure, which is common for the mesostructure-controlled sample.[36] The dispersive particles are better immersed in electrolyte, which will effectively shorten the lithium diffusion distance during the charge and discharge process. Activation process is thus not observed for the sample without mesostructure control. It should be noted that unlike the 20 μm size large secondary particles commonly obtained from the coprecipitation method by adding ammonia, our 3 μm size spherical particles have less kinetic limitations, which allows the material to cycle at higher current. No obvious capacity fading and voltage degradation is found for the mesostructure-controlled sample even after 150 cycles, whereas the sample synthesized by the CCP method encounters serious capacity fading and voltage degradation, although the initial capacity is close to that of the sample synthesized through the MCP method.

The improved cycling performance of the sample synthesized by the MCP method can be discussed in two aspects: (1) the mesostructure-controlled sample has almost 2-fold smaller surface area compared with the sample without mesostructure control (Table 2), which can effectively reduce side reactions between electrode surface and electrolyte species.[10] A thinner solid electrolyte interface layer is thus expected to form on the mesostructure-controlled particles surface, that enables a minimized capacity and voltage fading during cycling process; Figure 4g, h show the Nyquist plots of the cells prepared using the sample with and without mesostructure control before and after 30 cycles at a 0.1 C rate, as well as the corresponding equivalent circuit to fit the plots. R_s, R_{sei}, and R_{ct} represent electrolyte resistance, solid electrolyte interface (SEI) resistance, and charge transfer resistance, respectively. It turns out all the above resistance of the mesostructure-controlled sample does not increase obviously during the cycling process. The R_{sei} and R_{ct} values for the mesostructure-controlled sample even decrease from 3.8 to 3.5 Ω and from 40.6 to 39.5 Ω, respectively (see Table S1). This also well explains the increasing capacity over cycles of the mesostructure-controlled sample during the galvanostatic test. (2) uniformly distributed small secondary particles (~3 μm) possess increased structure mechanical stability so that no cracks can easily occur within the secondary particles, which will introduce less stress to the whole system.

3.3. 3D TXM Analysis. To evaluate the designed mesostructure mechanical stability upon cycling, we performed TXM measurements on both pristine and cycled electrodes for the sample synthesized by the MCP method. The total imaging volume is collected based on a field of view of 40 × 40 μm^2 with angular range of 180° (see Figure 5a, c). The data analysis was conducted after cropping a central volume of ~21 000 μm^3 from the total reconstruction as illustrated in Figure S5. On the basis of the 2D representative reconstructed slice, the mesostructure-controlled material has a certain amount of pores inside of the secondary particles for the pristine state, which is obviously different from the sample prepared by the coprecipitation method with adding ammonia (see Figure S6c). It is found by Yan et al. that the large size spherical particles assembled with densely packed crystallites introduce intergranular cracking after cycling, although these particles offer advantages for high energy density.[37] While, the pores between particles of the sample synthesized through the MCP method can effectively release the strain resulting from crystal lattice volumetric changes during battery cycling. As a result, the mesostructure-controlled material still maintains the spherical shape with ~3 μm in diameter even after 100 cycles at 0.1 C rate. For comparison, fragmentation of primary particles due to progressive internal cracking were observed

after only 50 cycles for the large size secondary particles (see Figure S6c, d).[38] Cracks that can be caused by the rough surface with high stress concentrations have been taken to be an important cycling performance degradation factor.[38] Different from the secondary particles with 10−20 μm, no serious cracks appear within the secondary particles synthesized through the MCP method after longer term cycling. Instead, more internal pores are indeed present in the cycled spherical secondary particles, resulting from strain release process during electrochemical cycling.

To carefully examine the mesostructural changes, the 3D reconstruction of a representative secondary particle is shown in Figure 6 for both pristine and cycled electrodes of the
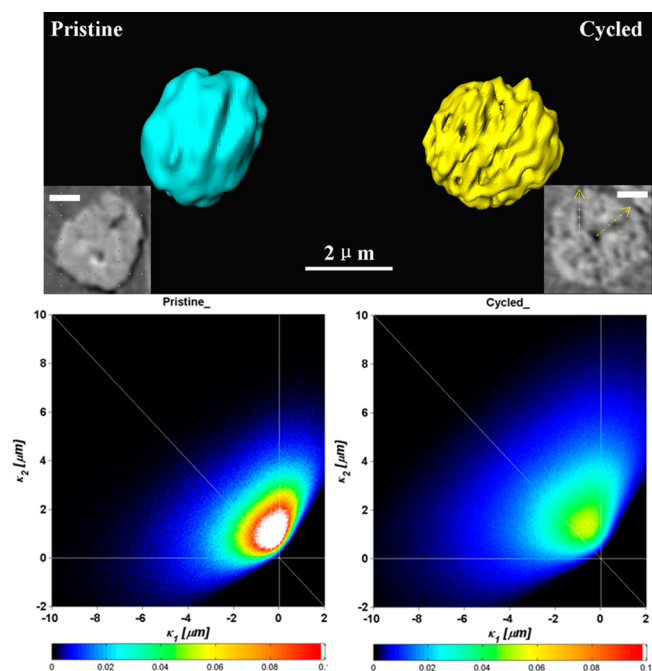

Figure 6. TXM reconstruction (upper panel) and curvature distribution maps (lower panel) of Li-rich layered oxide Li$_{1.2}$Ni$_{0.2}$Mn$_{0.6}$O$_2$ synthesized by the MCP method for the pristine electrode and cycled electrode. Inset of upper panel is 2D slice of the TXM reconstructed particles and the scale bar is 1 μm.

sample synthesized by the MCP method. Similar to the observation on a larger scale, no morphological changes are discernible after cycling except for pores or "channel-like" structure formation within the secondary particles as indicated by the arrows in the sliced 2D images. Specific surface area density was then calculated from the 3D images as described by Wilson et al.[39] Analysis of the specific surface area of all the particles within the total reconstruction volume is given in Table 3. After 100 cycles, the specific surface area is increased

Table 3. Microstructural Parameters Calculated from the 3D Reconstructed Pristine and Cycled Electrodes of Li-Rich Layered Oxide Li$_{1.2}$Ni$_{0.2}$Mn$_{0.6}$O$_2$ Synthesized by the MCP Method

sample	total reconstruction volume (μm³)	LNMO volume (μm³)	total surface area (μm²)	specific surface area (μm⁻¹)
pristine	21104	686.2	3100	4.5
cycled	22613	1460.9	9221.2	6.31

from 4.5 to 6.31 μm⁻¹ due to the channel formation that results in less agglomeration of the primary particles. The enhanced interfacial area could shorten the lithium diffusion distance, which improves battery performance after initial cycles and partially explains the activation process. Nevertheless, upon long cycling, the increased interfacial area will lead to more cathode electrolyte side reactions, causing impedance increase.

"Interfacial shape distribution (isd)" maps, also known as curvature distribution maps, are also generated in Figure 6. The principal curvature calculations were performed using "parallel surface method" developed by Jinnai et al.[40] In this method, a parallel surface is created via translating the interface by equal distance along its normal direction. The area of the parallel surface depends on the parallel displacement and the interfacial curvatures. The interfacial curvatures were thus deduced from the surface area by variation of parallel displacement. Generally, particle's surface with larger curvature feature develops much higher stress.[41] This high stress leads to fracture and pulverization of the particles, which finally causes voltage and capacity degradation during long-term cycling. As shown in Figure 6, the minimum and maximum principal curvatures at each point of particle surface, κ_1 and κ_2, form the probability density map (ISD map). The curvature of the particles surface is slightly increased after cycling indicating a less smooth surface, which could be due to the formation of channels. The distributions of two principal curvatures based on all particles from the pristine and cycled electrodes are shown in Table 4, which represents the convex and concave

Table 4. Quantitative Analysis of Curvature Distributions from the 3D Reconstructed Pristine and Cycled Electrodes of Li-Rich Layered Oxide Li$_{1.2}$Ni$_{0.2}$Mn$_{0.6}$O$_2$ Synthesized by the MCP Method

sample	convex (%)	saddle (%)	concave (%)
pristine	24.3	66.1	9.6
cycled	20	70.3	9.7

features in a statistical sense. It confirms that geometric characteristics do not change significantly after cycling in terms of the number of convex, saddle, and concave features. These results once more manifest the stable mesostructure of the sample synthesized through the MCP method. The overall spherical mesostructure is well preserved without formation of rough surface with high stress or cracks inside the secondary particles, which minimizes the voltage decay and capacity loss during electrochemical cycling for Li-rich layered oxide materials.

■ CONCLUSIONS

An MCP method has been developed to synthesize mesostructure-controlled Li-rich layered oxide material. Different from the coprecipitation method with adding ammonia, MCP method produces smaller secondary particles with diameter ∼3 μm. Though sacrificing some tap density, the designed mesostructure is more mechanically stable during electrochemical cycling compared with the secondary particles with 10−20 μm. Spherical shape secondary particles still well maintain without generating internal cracks and high stress after cycling. These observations indicate a balance between tap density and structure stability needs to be considered for optimization of this class of materials synthesized by

coprecipitation method. Additionally, the designed mesostructure has a much smaller surface area compared with the sample with dispersive particles. Consequently, no obvious capacity fading and voltage degradation is observed for the mesostructure-controlled sample even after 150 cycles, which shows the MCP method is promising for minimizing the capacity and voltage fading problem during cycling of Li-rich layered material. Long cycling duration of these materials still needs to be optimized based on the atomic structure transformation to fully suppress the voltage decay and capacity fading.

■ ASSOCIATED CONTENT

⑤ Supporting Information

The Supporting Information is available free of charge on the ACS Publications website at DOI: 10.1021/acsaem.8b00545.

> Additional information regarding descriptions of the XRD, SEM, electrochemical cycling profiles, corresponding dQ/dV plots, cropped segmented reconstruction volume, and 2D representative reconstructed slice of Li-rich layered oxide $Li_{1.2}Ni_{0.2}Mn_{0.6}O_2$ (PDF)

■ AUTHOR INFORMATION

Corresponding Author

*E-mail: shmeng@ucsd.edu.

ORCID ⑩

Ying Shirley Meng: 0000-0001-8936-8845

Author Contributions

Y.S.M. and M.Z. conceived the idea. M.Z., H.L., and C.F. performed materials synthesis and electrochemical experiments. Z.L. and M.Z. performed TXM experiments and analysis. All authors contributed to the writing of the manuscript and have given approval to the final version of the manuscript.

Notes

The authors declare no competing financial interest.

■ ACKNOWLEDGMENTS

■ REFERENCES

(1) Qiu, B.; Zhang, M.; Xia, Y.; Liu, Z.; Meng, Y. S. Understanding and Controlling Anionic Electrochemical Activity in High-Capacity Oxides for Next Generation Li-Ion Batteries. *Chem. Mater.* **2017**, *29* (3), 908−915.

(2) Assat, G.; Foix, D.; Delacourt, C.; Iadecola, A.; Dedryvère, R.; Tarascon, J.-M. Fundamental Interplay between Anionic/cationic Redox Governing the Kinetics and Thermodynamics of Lithium-Rich Cathodes. *Nat. Commun.* **2017**, *8* (1), 2219.

(3) Luo, K.; Roberts, M. R.; Hao, R.; Guerrini, N.; Pickup, D. M.; Liu, Y.-S.; Edström, K.; Guo, J.; Chadwick, A. V.; Duda, L. C.; Bruce, P. G. Charge-Compensation in 3d-Transition-Metal-Oxide Intercalation Cathodes through the Generation of Localized Electron Holes on Oxygen. *Nat. Chem.* **2016**, *8* (7), 684−691.

(4) Seo, D.-H.; Lee, J.; Urban, A.; Malik, R.; Kang, S.; Ceder, G. The Structural and Chemical Origin of the Oxygen Redox Activity in Layered and Cation-Disordered Li-Excess Cathode Materials. *Nat. Chem.* **2016**, *8* (7), 692−697.

(5) Qiu, B.; Zhang, M.; Wu, L.; Wang, J.; Xia, Y.; Qian, D.; Liu, H.; Hy, S.; Chen, Y.; An, K.; Zhu, Y.; Liu, Z.; Meng, Y. S. Gas−solid Interfacial Modification of Oxygen Activity in Layered Oxide Cathodes for Lithium-Ion Batteries. *Nat. Commun.* **2016**, *7*, 12108.

(6) Arunkumar, T. A.; Wu, Y.; Manthiram, A. Factors Influencing the Irreversible Oxygen Loss and Reversible Capacity in Layered $Li[Li1/3Mn2/3]O2−Li[M]O2$ (M = Mn0.5-yNi0.5-yCo2y and Ni1-yCoy) Solid Solutions. *Chem. Mater.* **2007**, *19* (12), 3067−3073.

(7) Ito, A.; Li, D.; Ohsawa, Y.; Sato, Y. A New Approach to Improve the High-Voltage Cyclic Performance of Li-Rich Layered Cathode Material by Electrochemical Pre-Treatment. *J. Power Sources* **2008**, *183* (1), 344−346.

(8) Mohanty, D.; Kalnaus, S.; Meisner, R. A.; Rhodes, K. J.; Li, J.; Payzant, E. A.; Wood, D. L.; Daniel, C. Structural Transformation of a Lithium-Rich Li1.2Co0.1Mn0.55Ni0.15O2 Cathode during High Voltage Cycling Resolved by in Situ X-Ray Diffraction. *J. Power Sources* **2013**, *229*, 239−248.

(9) Bettge, M.; Li, Y.; Gallagher, K.; Zhu, Y.; Wu, Q.; Lu, W.; Bloom, I.; Abraham, D. P. Voltage Fade of Layered Oxides: Its Measurement and Impact on Energy Density. *J. Electrochem. Soc.* **2013**, *160* (11), A2046−A2055.

(10) Hy, S.; Liu, H.; Zhang, M.; Qian, D.; Hwang, B.-J.; Meng, Y. S. Performance and Design Considerations for Lithium Excess Layered Oxide Positive Electrode Materials for Lithium Ion Batteries. *Energy Environ. Sci.* **2016**, *9* (6), 1931−1954.

(11) Peng, L.; Zhu, Y.; Chen, D.; Ruoff, R. S.; Yu, G. Two-Dimensional Materials for Beyond-Lithium-Ion Batteries. *Adv. Energy Mater.* **2016**, *6* (11), 1600025.

(12) Zhao, Y.; Peng, L.; Liu, B.; Yu, G. Single-Crystalline LiFePO₄ Nanosheets for High-Rate Li-Ion Batteries. *Nano Lett.* **2014**, *14* (5), 2849−2853.

(13) Peng, L.; Zhu, Y.; Khakoo, U.; Chen, D.; Yu, G. Self-Assembled LiNi1/3Co1/3Mn1/3O2 Nanosheet Cathodes with Tunable Rate Capability. *Nano Energy* **2015**, *17*, 36−42.

(14) Cho, T.; Park, S.; Yoshio, M. Preparation of Layered Li[Ni1/3Mn1/3Co 1/3]O2 as a Cathode for Lithium Secondary Battery by Carbonate Coprecipitation Method. *Chem. Lett.* **2004**, *33* (6), 704−705.

(15) Park, S.-M.; Cho, T.-H.; Yoshio, M. Novel Synthesis Method for Preparing Layered Li[Mn1/2Ni1/2]O2 as a Cathode Material for Lithium Ion Secondary Battery. *Chem. Lett.* **2004**, *33* (6), 748−749.

(16) Lee, D.-K.; Park, S.-H.; Amine, K.; Bang, H. J.; Parakash, J.; Sun, Y.-K. High Capacity Li[Li0.2Ni0.2Mn0.6]O2 Cathode Materials via a Carbonate Co-Precipitation Method. *J. Power Sources* **2006**, *162* (2), 1346−1350.

(17) Chen, L.; Su, Y.; Chen, S.; Li, N.; Bao, L.; Li, W.; Wang, Z.; Wang, M.; Wu, F. Hierarchical Li1.2Ni0.2Mn0.6O2 Nanoplates with Exposed {010} Planes as High-Performance Cathode Material for Lithium-Ion Batteries. *Adv. Mater.* **2014**, *26* (39), 6756−6760.

(18) Li, L.; Song, S.; Zhang, X.; Chen, R.; Lu, J.; Wu, F.; Amine, K. Ultrasonic-Assisted Co-Precipitation to Synthesize Lithium-Rich Cathode Li1.3Ni0.21Mn0.64O2+d Materials for Lithium-Ion Batteries. *J. Power Sources* **2014**, *272*, 922−928.

(19) Park, S.-H.; Kang, S.-H.; Belharouak, I.; Sun, Y. K.; Amine, K. Physical and Electrochemical Properties of Spherical Li1+x(Ni1/3Co1/3Mn1/3)1−xO2 Cathode Materials. *J. Power Sources* **2008**, *177* (1), 177−183.

(20) Wang, D.; Belharouak, I.; Ortega, L. H.; Zhang, X.; Xu, R.; Zhou, D.; Zhou, G.; Amine, K. Synthesis of High Capacity Cathodes for Lithium-Ion Batteries by Morphology-Tailored Hydroxide Co-Precipitation. *J. Power Sources* **2015**, *274*, 451−457.

(21) Wang, D.; Belharouak, I.; Koenig, G. M.; Zhou, G.; Amine, K. Growth Mechanism of Ni0.3Mn0.7CO3 Precursor for High Capacity Li-Ion Battery Cathodes. *J. Mater. Chem.* **2011**, *21* (25), 9290−9295.

(22) Oh, P.; Myeong, S.; Cho, W.; Lee, M.-J.; Ko, M.; Jeong, H. Y.; Cho, J. Superior Long-Term Energy Retention and Volumetric Energy Density for Li-Rich Cathode Materials. *Nano Lett.* **2014**, *14* (10), 5965−5972.

(23) Chen, C.-J.; Pang, W. K.; Mori, T.; Peterson, V. K.; Sharma, N.; Lee, P.-H.; Wu, S.; Wang, C.-C.; Song, Y.-F.; Liu, R.-S. The Origin of Capacity Fade in the Li2MnO3·LiMO2 (M = Li, Ni, Co, Mn) Microsphere Positive Electrode: An Operando Neutron Diffraction and Transmission X-Ray Microscopy Study. *J. Am. Chem. Soc.* **2016**, *138* (28), 8824−8833.

(24) Chen, W.-C.; Song, Y.-F.; Wang, C.-C.; Liu, Y.; Morris, D. T.; Pianetta, P. A.; Andrews, J. C.; Wu, H.-C.; Wu, N.-L. Study on the Synthesis−microstructure-Performance Relationship of Layered Li-Excess Nickel−manganese Oxide as a Li-Ion Battery Cathode Prepared by High-Temperature Calcination. *J. Mater. Chem. A* **2013**, *1* (36), 10847−10856.

(25) Liu, H.; Qian, D.; Verde, M. G.; Zhang, M.; Baggetto, L.; An, K.; Chen, Y.; Carroll, K. J.; Lau, D.; Chi, M.; Veith, G. M.; Meng, Y. S. Understanding the Role of NH4F and Al2O3 Surface Co-Modification on Lithium-Excess Layered Oxide Li1.2Ni0.2Mn0.6O2. *ACS Appl. Mater. Interfaces* **2015**, *7* (34), 19189−19200.

(26) Wang, J.; Karen Chen, Y.; Yuan, Q.; Tkachuk, A.; Erdonmez, C.; Hornberger, B.; Feser, M. Automated Markerless Full Field Hard X-Ray Microscopic Tomography at Sub-50 Nm 3-Dimension Spatial Resolution. *Appl. Phys. Lett.* **2012**, *100* (14), 143107−143110.

(27) Natterer, F. *The Mathematics of Computerized Tomography*; B.G. Teubner: Stuttgart, Germany, 1986.

(28) Chen-Wiegart, Y. K.; Liu, Z.; Faber, K. T.; Barnett, S. A.; Wang, J. 3D Analysis of a LiCoO2−Li(Ni1/3Mn1/3Co1/3)O2 Li-Ion Battery Positive Electrode Using X-Ray Nano-Tomography. *Electrochem. Commun.* **2013**, *28*, 127−130.

(29) Ngala, J. K.; Chernova, N. A.; Ma, M.; Mamak, M.; Zavalij, P. Y.; Whittingham, M. S. The Synthesis, Characterization and Electrochemical Behavior of the Layered LiNi0.4Mn0.4Co0.2O2 Compound. *J. Mater. Chem.* **2004**, *14* (2), 214−220.

(30) Hwang, B. J.; Tsai, Y. W.; Carlier, D.; Ceder, G. A Combined Computational/Experimental Study on LiNi1/3Co1/3Mn1/3O2. *Chem. Mater.* **2003**, *15* (19), 3676−3682.

(31) Zhang, Y.; Xu, G.; Wei, X.; Ren, Z.; Liu, Y.; Shen, G.; Han, G. Hydrothermal Synthesis, Characterization and Formation Mechanism of Self-Assembled Mesoporous SrTiO3 Spheres Assisted with Na2SiO3·9H2O. *CrystEngComm* **2012**, *14* (10), 3702.

(32) Euliss, L. E.; Grancharov, S. G.; O'Brien, S.; Deming, T. J.; Stucky, G. D.; Murray, C. B.; Held, G. A. Cooperative Assembly of Magnetic Nanoparticles and Block Copolypeptides in Aqueous Media. *Nano Lett.* **2003**, *3* (11), 1489−1493.

(33) Fu, C.; Ravindra, N. M. Magnetic Iron Oxide Nanoparticles: Synthesis and Applications. *Bioinspired, Biomimetic Nanobiomater.* **2012**, *1* (4), 229−244.

(34) Liu, H.; Chen, Y.; Hy, S.; An, K.; Venkatachalam, S.; Qian, D.; Zhang, M.; Meng, Y. S. Operando Lithium Dynamics in the Li-Rich Layered Oxide Cathode Material via Neutron Diffraction. *Adv. Energy Mater.* **2016**, *6* (7), 1502143.

(35) Armstrong, A. R.; Holzapfel, M.; Novák, P.; Johnson, C. S.; Kang, S.-H.; Thackeray, M. M.; Bruce, P. G. Demonstrating Oxygen Loss and Associated Structural Reorganization in the Lithium Battery Cathode Li[Ni0.2Li0.2Mn0.6]O2. *J. Am. Chem. Soc.* **2006**, *128* (26), 8694−8698.

(36) Zhang, J.; Guo, X.; Yao, S.; Zhu, W.; Qiu, X. Tailored Synthesis of Ni0.25Mn0.75CO3 Spherical Precursors for High Capacity Li-Rich Cathode Materials via a Urea-Based Precipitation Method. *J. Power Sources* **2013**, *238*, 245−250.

(37) Yan, P.; Zheng, J.; Gu, M.; Xiao, J.; Zhang, J.-G.; Wang, C.-M. Intragranular Cracking as a Critical Barrier for High-Voltage Usage of Layer-Structured Cathode for Lithium-Ion Batteries. *Nat. Commun.* **2017**, *8*, 14101.

(38) Song, B.; Sui, T.; Ying, S.; Li, L.; Lu, L.; Korsunsky, A. M. Nano-Structural Changes in Li-Ion Battery Cathodes during Cycling Revealed by FIB-SEM Serial Sectioning Tomography. *J. Mater. Chem. A* **2015**, *3* (35), 18171−18179.

(39) Wilson, J. R.; Cronin, J. S.; Duong, A. T.; Rukes, S.; Chen, H.-Y.; Thornton, K.; Mumm, D. R.; Barnett, S. Effect of Composition of (La0.8Sr0.2MnO3−Y2O3-Stabilized ZrO2) Cathodes: Correlating Three-Dimensional Microstructure and Polarization Resistance. *J. Power Sources* **2010**, *195* (7), 1829−1840.

(40) Jinnai, H.; Koga, T.; Nishikawa, Y.; Hashimoto, T.; Hyde, S. T. Curvature Determination of Spinodal Interface in a Condensed Matter System. *Phys. Rev. Lett.* **1997**, *78* (11), 2248−2251.

(41) Lim, C.; Yan, B.; Yin, L.; Zhu, L. Simulation of Diffusion-Induced Stress Using Reconstructed Electrodes Particle Structures Generated by Micro/nano-CT. *Electrochim. Acta* **2012**, *75*, 279−287.